

Spectroscopic properties of dipicolinic acid and its dianion

John Rui-Hua Xie ^a, Vedene H. Smith Jr. ^b, Roland E. Allen ^{a,*}

^a Department of Physics and Institute for Quantum Studies, Texas A&M University, College Station, TX 77843-4242, United States

^b Department of Chemistry, Queen's University, Kingston, Ont., Canada K7L 3N6

Received 13 May 2005; accepted 17 August 2005

Available online 7 October 2005

Abstract

If robust spectroscopic techniques are to be developed for the detection and identification of pathogens, one must understand the relevant spectroscopic properties of the target molecules. In this paper, we employ density functional theory (DFT) to study the structural, electronic, vibrational, optical, and magnetic properties of dipicolinic acid (DPA) and its dianion DPA^{-2} . Our full geometrical optimization and Mulliken charge analysis show that DFT does not lead to the significant discrepancies between charges on symmetric carbon, hydrogen, and oxygen atoms that are found in less accurate calculations based on the complete active space MCSCF method. Our calculated vibrational frequencies, Raman spectra, and infrared spectra for ground-state DPA and DPA^{-2} are in good agreement with experiment, and this is also true of the four calculated ^{13}C NMR spectral lines (for α , β , γ , and carboxyl sites). Our time-dependent DFT study of the optical excitation and absorption of both DPA and DPA^{-2} provides the first interpretation of the observed near ultraviolet absorption and fluorescence spectra. Finally, we discuss for the first time the effect of a solvent on the spectral properties of DPA. © 2005 Elsevier B.V. All rights reserved.

Keywords: Dipicolinic acid; Spectroscopic properties; Optical excitation; Raman spectra; Infrared spectra; Vibrational frequencies

1. Introduction

Dipicolinic acid (DPA, also designated 2,6-pyridinedicarboxylic acid or $\text{C}_5\text{H}_3\text{N}(\text{COOH})_2$) has the structure shown in Fig. 1. It was first discovered in a biological system in 1936 [1], and is now known to be a major component of bacterial spores [2,3]. This substance appears to contribute to the resistance of the spores to UV radiation [4] and to be important for their stability and germination. The dianion DPA^{-2} , in which the two hydrogen nuclei at sites 16 and 17 are removed from DPA, occurs in salts like calcium dipicolinate, which are also found in the spores.

Spectroscopic approaches for rapidly detecting and identifying bacterial spores have been proposed and are currently being developed. We mention in particular FAST CARS (femtosecond adaptive spectroscopic technique

using coherent anti-Stokes Raman scattering) [5,6], which has demonstrated promise for rapid detection of small samples. Experiments have shown that the UV absorption spectra of various bacterial spores are similar to those of DPA and its anion [7], and that the Raman spectra of spores exhibit strong evidence of calcium dipicolinate [8–11].

To assist with the development of robust spectroscopic methods, one needs reliable theoretical tools for accurately describing bacterial spores, and for interpreting and identifying their spectral properties. To our knowledge, the only previous theoretical analysis of the vibrational frequencies of DPA and DPA^{-2} was based on the CASSCF (complete active space MCSCF) method [3]. This work relied on empirical correction factors to provide better assignments for comparison with experiment, and also led to significant discrepancies in the predicted charges of the symmetric carbon, oxygen, and hydrogen atoms. For example, the charges on C9 and C10 in ground-state DPA^{-2} should be the same, but CASSCF gave 0.742e and 0.669e.

* Corresponding author. Tel.: +1 979 845 4341; fax: +1 979 845 2590.
E-mail address: allen@tamu.edu (R.E. Allen).

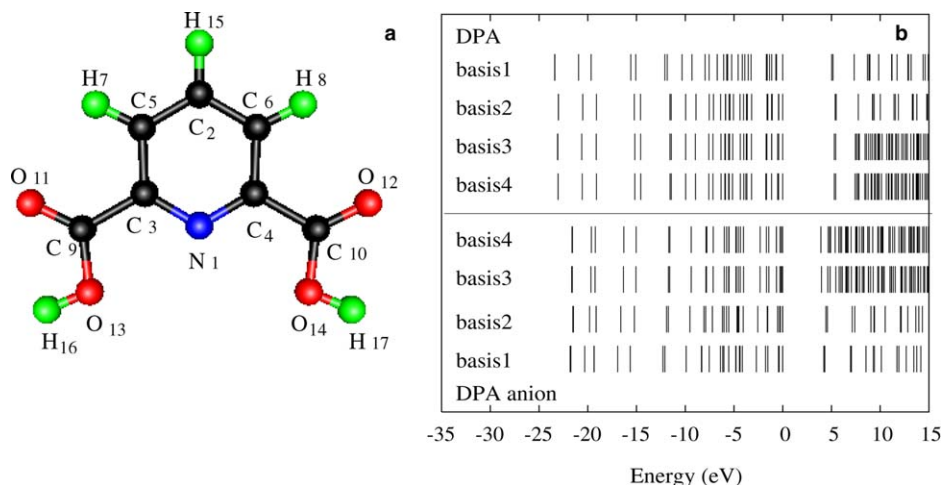


Fig. 1. Left: Geometric structure of DPA optimized using B3LYP/6-311+G(2df,2pd). The site numbers are labeled. Right: Detailed orbital energies computed with 4 different basis sets: basis1: 6-31G; basis2: 6-31G(d,p); basis3: 6-311+G(d,p); basis4: 6-311+G(2df,2pd).

Previous theoretical studies have also used relatively small basis sets: for example, 3-21G [2] and 6-31G [3]. However, both DPA and its anion have electron lone pairs, and are in excited states after exposure to UV radiation. One should, therefore, add polarization and diffuse functions to obtain an accurate description of DPA and DPA^{-2} . This kind of basis set, e.g., 6-311+G(d,p), is appropriate for systems with lone pairs, anions, and excited states. Taking the H_2 molecule as an example, time-dependent density functional theory (TD-DFT) [12] with a hybrid B3LYP functional [13] shows that the lowest excited energy ($^1\Sigma_u^+$ singlet state) at $R = 1.4$ bohr is found to be, respectively, 25.289, 15.321, 14.770, 14.621, 12.920, 12.942, and 12.611 eV with STO-3G, 3-21G, 6-31G, 6-31G(d,p), 6-311+G(d,p), 6-311+G(2df,2pd), and 6-311+G(3df,3pd) basis sets, whereas the exact value is 12.796 eV [14].

Here, we report a systematic study, using density functional theory (DFT), of the spectral properties of both DPA and DPA^{-2} , including the Raman, infrared (IR), near ultraviolet, and NMR spectra. We also discuss the effects of basis sets, which play an important role as discussed above. Finally, we report calculations for DPA in solution as well as in the gas phase, since many of the experiments involve, e.g., Raman spectra of DPA in water [10]. We find that DFT provides a good description of all these different aspects of the spectroscopic properties of DPA, as well as the bond lengths and vibrational frequencies.

2. Ground-state structure and total energy

In the present paper, we focus on the properties of DPA and DPA^{-2} in their ground-state structures. (Again, 2 hydrogen nuclei at sites 16 and 17, as shown in Fig. 1, are removed from DPA in the anion, which is found in salts like calcium dipicolinate. In a subsequent paper, we will discuss the lowest singlet excited-state structures.) The

geometries of ground-state DPA and DPA^{-2} were fully optimized, using DFT with the B3LYP hybrid functional [13], and exploiting the analytical calculation of first-order energy derivatives. The same methodology was used to calculate the harmonic vibrational frequencies reported in Sections 3 and 6. We used the Gaussian03 package with Pople-type Gaussian basis sets [15], and we extensively tested the effects of employing different double-zeta basis sets: 6-31G (2 sets of functions in the valence region and 1 set in the core), 6-31G(d,p) (adding polarization functions to the atoms), 6-311+G(d,p) (also adding diffuse functions, which are important for systems with lone pairs, anions, and excited states), and 6-311+G(2df,2pd) (additionally putting 2d functions and 1f function on heavy atoms, or 2p functions and 1d function on hydrogen).

We now turn to the results, beginning with Fig. 1, which shows the geometry of DPA optimized with B3LYP/6-311+G(2df,2pd). All detailed results for ground-state DPA and DPA^{-2} are summarized in Tables 1–4, which list the total energies, Mulliken charges, bond lengths, and bond angles.

Table 1

Total energies E (in eV) relative to that calculated with B3LYP/6-311+G(2df,2pd); LUMO–HOMO gap E_δ (in eV); and the average of the diagonal elements of the static polarizability α (in \AA^3)

Material	6-31G	6-31G (d,p)	6-311+G (d,p)	6-311+G (2df,2pd)	CASSCF
DPA					
E	11.949	5.905	1.034	0.000	107.157
E_δ	5.019	5.375	5.301	5.301	–
α	80	87	101	103	–
DPA^{-2}					
E	12.381	7.184	0.925	0.000	108.790
E_δ	4.225	4.428	3.979	3.928	–
α	82	86	124	126	–

The CASSCF results are taken from [3].

Table 2
B3LYP/6-311+G(2df,2pd) calculations of Mulliken charges in DPA and DPA⁻²

Atom	DPA		DPA ⁻²	
	B3LYP	CASSCF	B3LYP	CASSCF
N1	-0.14035 (-0.21739, -0.20331)	-0.48151	-0.17560	-0.54342
C2	-0.45372 (-0.48849, -0.48418)	-0.18960	-0.43191	-0.18729
C3	0.08434 (0.12280, 0.11298)	0.11871	-0.14491	0.08179
C4	0.08434 (0.12326, 0.11302)	0.11863	-0.14491	0.09886
C5	0.17834 (0.19878, 0.19749)	-0.13432	0.08074	-0.21124
C6	0.17834 (0.19809, 0.19245)	-0.13428	0.08074	-0.19890
H7	0.09198 (0.10559, 0.10471)	0.27096	0.04345	0.21024
H8	0.09198 (0.10562, 0.10471)	0.27096	0.04345	0.20826
C9	0.32536 (0.36273, 0.36702)	0.77401	0.42399	0.74203
C10	0.32536 (0.36308, 0.36702)	0.77424	0.42399	0.66944
O11	-0.43267 (-0.51540, -0.51244)	-0.55176	-0.56050	-0.81241
O12	-0.43267 (-0.51548, -0.51243)	-0.55200	-0.56050	-0.79461
O13	-0.20675 (-0.28174, -0.27471)	-0.70023	-0.54367	-0.73021
O14	-0.20675 (-0.28182, -0.27470)	-0.70012	-0.54367	-0.65900
H15	0.07139 (0.10374, 0.10191)	0.22770	0.09297	0.12646
H16	0.22074 (0.30830, 0.30273)	0.44432		
H17	0.22074 (0.30834, 0.30273)	0.44430		

The CASSCF results are taken from [3]. The values in parentheses are computed for DPA in water (first number) and in ethanol (second number), respectively.

Table 3
B3LYP/6-311+G(2df,2pd) calculations of bond lengths (in Å) in DPA and its dianion

Bond length	DPA		DPA dianion		
	B3LYP	CASSCF	B3LYP	CASSCF	Experimental
N1–C3	1.3301 (1.3325, 1.3322)	1.3377	1.3420	1.3382	1.35
N1–C4	1.3301 (1.3325, 1.3322)	1.3377	1.3420	1.3382	1.33
C2–C5	1.3864 (1.3864, 1.3865)	1.3950	1.3870	1.3883	1.40
C2–C6	1.3864 (1.3864, 1.3865)	1.3950	1.3870	1.3883	1.39
C3–C5	1.3952 (1.3949, 1.3950)	1.3983	1.4002	1.3956	1.39
C4–C6	1.3952 (1.3949, 1.3950)	1.3988	1.4002	1.3956	1.40
C3–C9	1.5011 (1.5021, 1.5020)	1.4837	1.5481	1.5353	1.49
C4–C10	1.5011 (1.5021, 1.5020)	1.4837	1.5481	1.5353	1.51
C9–O11	1.2075 (1.2140, 1.2139)	1.2157	1.2608	1.2757	1.26
C10–O12	1.2075 (1.2140, 1.2139)	1.2157	1.2608	1.2757	1.26
C9–O13	1.3405 (1.3297, 1.3301)	1.3361	1.2476	1.2517	1.24
C10–O14	1.3405 (1.3297, 1.3301)	1.3361	1.2476	1.2517	1.23
O13–H16	0.9680 (0.9917, 0.9900)	0.9545	1.0814	1.0689	–
O14–H17	0.9680 (0.9917, 0.9900)	0.9545	1.0814	1.0689	–
C5–H7	1.0795 (1.0825, 1.0823)	1.0697	1.0873	1.0779	–
C6–H8	1.0795 (1.0825, 1.0823)	1.0697			
C2–H15	1.0811 (1.0847, 1.0844)	1.0712			

The CASSCF results are taken from [3], and the experimental results from [16]. The values in parentheses are computed for DPA in water (first number) and in ethanol (second number), respectively.

Our results demonstrate the convergence of the total energy calculations for this molecule, using B3LYP methods, with respect to the basis sets. For both DPA and DPA⁻², the total energies calculated with the 6-31G, 6-31G(d,p), and 6-311+G(d,p) basis sets differ from that calculated with the largest basis set, 6-311+G(2df,2dp), by about 12, 6, and 1 eV, respectively. The convergence is also demonstrated by the orbital energies shown in Fig. 1, and the LUMO–HOMO gaps listed in Table 1. For comparison, Table 1 also lists the total energies of DPA and DPA⁻² computed using the CASSCF method [3]. Since Hamerka et al. [3] employed an incomplete active space, and used a small basis set which did not include the effects of polariza-

tion and diffuse functions, we find that the total energy calculated by them with CASSCF is about 108 eV (2510 kcal/mol) higher than that calculated with B3LYP/6-311+G(2df,2dp).

Our Mulliken charge analysis is given in Table 2 for DPA and DPA⁻², which both have 4 distinct kinds of carbon sites and 2 kinds of oxygen sites. In DPA, the nitrogen atom, the carbon atom at site 2, and the oxygen atoms act as electron acceptors, while carbon at the other sites and hydrogen act as electron donors. In particular, the hydrogen at sites 16 and 17, and the carbon at sites 9 and 10, donate more electronic charge than those at other hydrogen and carbon donor sites, while the oxygen atoms at sites

Table 4
B3LYP/6-311+G(2df,2pd) calculations of bond angles (in °) in DPA and its dianion

Bond angle	DPA		DPA dianion		Experimental
	B3LYP	CASSCF	B3LYP	CASSCF	
C5–C3–C9	118.07	118.67	117.64	117.74	115.1
C6–C4–C10	118.07	118.67	117.64	117.74	114.8
C2–C5–C3	118.40	118.50	119.02	119.05	117.4
C2–C6–C4	118.40	118.50	119.02	119.05	118.3
C5–C2–C6	118.82	118.93	118.94	119.12	118.3
N1–C3–C9	118.72	118.73	120.63	121.22	122.3
N1–C4–C10	118.72	118.73	120.63	121.22	122.6
N1–C3–C5	123.22	122.59	121.73	121.04	122.5
N1–C4–C6	123.22	122.59	121.73	121.04	122.6
C3–N1–C4	117.96	118.89	119.41	120.71	119.0
C3–C9–O11	123.04	122.61	114.30	114.31	117.0
C4–C10–O12	123.04	122.61	114.30	114.31	115.7
C3–C9–O13	113.67	115.21	117.10	119.03	117.8
C4–C10–O14	113.67	115.21	117.10	119.03	118.2
O11–C9–O13	123.30	122.18	128.53	126.66	125.2
O12–C10–O14	123.30	122.18	128.53	126.66	126.0
C2–C5–H7	122.22	121.93	122.28	123.02	–
C2–C6–H8	122.22	121.93	122.28	123.02	–
C3–C5–H7	119.38	119.58	118.70	117.93	–
C4–C6–H8	119.38	119.58	118.70	117.93	–
C5–C2–H15	120.60	120.53	120.53	120.44	–
C6–C2–H15	120.60	120.53	120.53	120.44	–
C9–O13–H16	106.75	113.33			
C10–O14–H17	106.75	113.33			

The CASSCF results are taken from [3], and the experimental results from [16].

11 and 12 accept more charge than those at sites 13 and 14. For the DPA dianion, the carbon atoms at sites 3 and 4 become additional electron acceptors, with all the oxygen atoms now acting as strong acceptors. Although a Mulliken charge analysis does not give quantitatively meaningful charges, our DFT calculations do lead to the physically correct prediction that there are symmetric charge distributions for symmetric C, O, and H atoms. In contrast, the CASSCF computation [3] led to asymmetric charges on symmetric C, O, and H atoms: for example, the charges on C9 and C10, O11 and O12, and C3 and C4. This feature raises some doubt about the accuracy and reliability of the CASSCF method for describing systems like DPA and DPA^{−2}. Also, the CASSCF results predict that the carbon atoms at sites 5 and 6 act as electron acceptors, and this is contradicted by our DFT results.

The optimized bond lengths in DPA and DPA^{−2} are shown in Table 3. In both DPA and DPA^{−2}, there are 3 types of C–C bonds, 2 types of O–C and C–H bonds, and 1 type of N–C bond. For DPA, there is also one type of O–H bond. As the basis set is increased from 6-31G, 6-31G(d,p), and 6-311+G(d,p) to 6-311+G(2df,2pd), the predicted bond lengths become smaller, but they are finally converged to within 0.2%, in the sense that the results for the last two basis sets differ by only this amount.

The computed bond angles for DPA and DPA^{−2} are listed in Table 4. We find that these angles are converged

from 0.1% to within 0.05% as we increase the size of the basis set from 6-31G, 6-31G(d,p) and 6-311+G(d,p) up to 6-311+G(2df,2pd). The calculated bond lengths and bond angles at first appear not to be in good agreement with the experimental results [16]. However, the theory is for molecules in the gas phase, while the experimental measurements are for molecules in solution. In the experiments, the bond lengths and angles lack symmetry, and there are especially large discrepancies in the bond angles of the carboxyl groups. This is due to their interaction with the calcium ions and the surrounding water molecules. In Section 6, we focus on issues involving solvent effects.

Finally, we consider the dependence of polarizabilities on the basis set. In Table 1, the isotropic static polarizabilities are presented for DPA and DPA^{−2}. As the basis set size is increased from 6-31G, 6-31G(d,p) and 6-311+G(d,p) up to 6-311+G(2df,2pd), the polarizability is converged from 22% to within 1%.

The above results demonstrate that the choice of basis set strongly affects the reliability of the calculations, and that one should include polarization and diffuse functions in DFT calculations for substances like DPA and DPA^{−2}.

3. Raman and infrared spectra

Raman and infrared (IR) spectroscopies are now standard tools for chemical characterization. The application of these techniques to complex systems is greatly assisted by quantum-chemical calculations of properties like normal-mode frequencies and band intensities.

The vibrational analysis of polyatoms described by Wilson et al. [17] has been widely employed in chemical physics and is implemented in the Gaussian03 package. This analysis is valid only when the first derivative of the energy with respect to each atomic displacement is zero. In other words, the geometry used in treating vibrations must be optimized with the same level of theory and the same basis set that are used to generate the second derivatives [18]. The force constant matrix \mathbf{K} is defined to contain the second derivatives of the potential V with respect to the atomic displacements. It is convenient to convert \mathbf{K} to a new matrix $\tilde{\mathbf{K}}$ [19] involving mass-weighted coordinates $q_i = m_i^{1/2}\eta_i$

$$\tilde{K}_{ij} \equiv (m_i m_j)^{-1/2} K_{ij} = \left(\frac{\partial^2 V}{\partial q_i \partial q_j} \right)_0, \quad (3.1)$$

where m_i is the atomic mass. Then the eigenvalues λ_k of $\tilde{\mathbf{K}}$ give the fundamental frequencies in cm^{-1} , $\tilde{\nu}_k = \lambda_k^{1/2}/(2\pi c)$ (where c is the speed of light in vacuum), and each eigenvector gives the character of the corresponding normal mode.

To lowest order, the IR intensities are given by the derivatives of the dipole moment \mathbf{P} with respect to the normal mode coordinates, evaluated in the equilibrium geometry. In detail, the IR intensity of the q th vibrational mode is given by [18]

$$I_{\text{ir}}^{(q)} = \frac{\rho_p \pi}{3c} \left| \frac{d\mathbf{P}}{d\varepsilon_q} \right|^2, \quad (3.2)$$

where ρ_p is the particle density and ε_q is the normal mode coordinate for the q th mode. Since $|d\mathbf{P}/d\varepsilon_q|$ is the only molecular property entering the formula, it is often referred to as the absolute IR intensity.

The calculation of Raman intensities for isolated molecules is usually done via the following procedure: In the Born–Oppenheimer approximation, assume that the electronic ground state is non-degenerate and that the exciting frequency is much less than each relevant electronic frequency in the molecule. Then the Raman intensities can be expressed in terms of the derivatives of the dynamic polarizability with respect to the normal mode coordinates (evaluated in the equilibrium geometry). For example, most Raman scattering experiments use a plane-polarized incident laser beam. The direction of the incident beam, the direction of its polarization, and the direction toward the detector are chosen to be perpendicular to one other. Under these circumstances, the first-order differential cross section for Raman scattering in the q th vibrational mode is written as [19]

$$\left(\frac{d\sigma}{d\Omega} \right)_q = \frac{\hbar\omega_s^4}{90c^4\pi\omega_q(1-n_q)} I_r, \quad (3.3)$$

where I_r is the Raman scattering activity, $n_q = \exp[-\hbar\omega_q/(\kappa_B T)]$, ω_s is the frequency of the scattered radiation, ω_q is the frequency of the q th vibrational mode, κ_B is Boltzmann's constant, and T is the temperature. For the special case of a $\pi/2$ scattering geometry, I_r can be written as [19]

$$I_r = 5 \left(\frac{d\alpha_{xx}}{d\varepsilon_q} + \frac{d\alpha_{yy}}{d\varepsilon_q} + \frac{d\alpha_{zz}}{d\varepsilon_q} \right)^2 + \frac{7}{4} \left[\left(\frac{d\alpha_{xx}}{d\varepsilon_q} - \frac{d\alpha_{yy}}{d\varepsilon_q} \right)^2 + \left(\frac{d\alpha_{xx}}{d\varepsilon_q} - \frac{d\alpha_{zz}}{d\varepsilon_q} \right)^2 + \left(\frac{d\alpha_{yy}}{d\varepsilon_q} - \frac{d\alpha_{zz}}{d\varepsilon_q} \right)^2 + 6 \left(\frac{d\alpha_{xy}}{d\varepsilon_q} \right)^2 + 6 \left(\frac{d\alpha_{xz}}{d\varepsilon_q} \right)^2 + 6 \left(\frac{d\alpha_{yz}}{d\varepsilon_q} \right)^2 \right], \quad (3.4)$$

where α is the dipole polarizability tensor. It should be mentioned that the above equation is valid only if resonant effects are neglected.

To obtain the IR properties, one must compute the derivatives of the dipole moment with respect to the normal mode coordinates. These can be viewed as directional derivatives in the space of $3N$ nuclear coordinates, and are expressed in terms of derivatives with respect to atomic coordinates R_k . For the i th component of the dipole moment \mathbf{P} ($i = x, y, z$), we have [18]

$$\frac{d\mathbf{P}_i}{d\varepsilon_q} = \sum_{k=1}^{3N} \frac{\partial \mathbf{P}_i}{\partial R_k} \xi_{kq}, \quad (3.5)$$

where $\xi_{kq} = \partial R_k / \partial \varepsilon_q$ is the k th atomic displacement in the q th normal mode. Then the necessary derivatives can be expressed in terms of the atomic forces as follows [18]:

$$\frac{\partial \mathbf{P}_i}{\partial R_k} = - \frac{\partial^2 E}{\partial G_i \partial R_k} = \frac{\partial F_k}{\partial G_i}, \quad (3.6)$$

where E is the total energy, G_i is the i th component of an assumed external electric field \mathbf{G} , and F_k is the calculated force on the k th atomic coordinate. Similarly, to obtain the Raman activities, one must compute the derivatives of the polarizability with respect to the normal mode coordinates ε_q . For the polarizability component α_{ij} ($i, j = x, y, z$), we have [19]

$$\frac{d\alpha_{ij}}{d\varepsilon_q} = \sum_{k=1}^{3N} \frac{\partial \alpha_{ij}}{\partial R_k} \xi_{kq}. \quad (3.7)$$

Then, the necessary derivatives can be expressed in terms of the atomic forces as follows [19]:

$$\frac{\partial \alpha_{ij}}{\partial R_k} = - \frac{\partial^3 E}{\partial G_i \partial G_j \partial R_k} = \frac{\partial^2 F_k}{\partial G_i \partial G_j}. \quad (3.8)$$

To do DFT calculations, we need to choose the exchange-correlation functional and basis sets. Hybrid DFT functionals have been shown to give good estimates for polarizabilities in the gas phase, and a good description of molecular vibrations. One therefore expects IR and Raman spectra to be accurately predicted. Here we use the B3LYP hybrid functional, and we investigate the dependence of the results on the choice of the basis set.

DPA (DPA⁻²) has a total of 17 (15) atoms and thus 45 (39) vibrational modes. In Table 5, we list their vibrational frequencies, as calculated with the hybrid B3LYP functional and with 6-311+G(2df,2pd) basis sets. It should be mentioned that no scaling factors have been employed in calculating the vibrational frequencies. The frequencies for DPA and DPA⁻² computed by CASSCF [3] and measured by several experimental groups [5,10,11] are also listed in Table 5 for comparison. The modes of DPA can be grouped into 31 in-plane and 14 out-of-plane vibrations. We have examined the detailed form of each vibrational mode using visual 3D software, and our mode assignments are the same as those of Hameka et al. [3]. We find that increasing the size of the basis set leads to converged vibrational frequencies. When compared to the measured frequencies for both DPA and DPA⁻², which are listed in Table 5, our DFT calculations show better overall agreement than those obtained with the CASSCF method [3]. For example, the relative error between the highest frequency (3991.6 cm⁻¹) predicted by CASSCF and experiment (3520 cm⁻¹) is 13%, while the relative error is 6% in B3LYP/6-311+G(2df,2pd) calculation.

In Table 5, we also list the Raman scattering activities and IR intensities for DPA and DPA⁻². These values are converged with respect to the size of the basis set. In Fig. 2, we show the Raman and IR spectra for DPA and DPA⁻² computed with B3LYP/6-311+G(2df,2pd). The most intense calculated IR-active frequencies for DPA include the O–H stretch mode at about 3761 cm⁻¹, the C=O stretch mode at about 1780 cm⁻¹, the C–H bend mode near 1231 cm⁻¹, the C–O stretch mode near

Table 5

B3LYP/6-311+G(2df,2pd) calculations of Raman scattering activities (I_r , in 10^{-14} m⁴/kg), infrared intensities (I_{ir} , in km/mol), and vibrational frequencies (ν , in cm⁻¹), for DPA and its dianion

DPA					DPA dianion				
CASSCF	Experimental	B3LYP			CASSCF	Experimental	B3LYP		
ν	ν	ν	I_r	I_{ir}	ν	ν	ν	I_r	I_{ir}
75.2	79	41.2	0.4	0.0	67.6	64	27.6	2.0	3.6
76.2	79	48.9	0.0	5.5	99.9	104	30.4	2.8	0.0
146.3	107	132.9	0.5	0.2	161.5	127	126.8	1.2	1.1
206.8	218	151.4	0.7	5.2	192.5	183	135.1	3.5	2.9
221.1	–	167.2	1.6	0.0	220.0	213	145.4	2.0	4.3
276.9	252	252.2	0.3	12.2	299.5	269	264.6	0.0	4.6
387.2	330	356.0	4.7	2.6	373.6	347	319.5	1.5	1.5
419.2	365	387.0	1.0	1.4	429.9	418	357.8	2.1	5.8
502.8	421	435.0	0.0	0.2	512.1	485	367.0	0.1	8.0
519.8	–	464.2	0.5	0.0	516.3	485	413.3	0.9	6.0
524.1	–	464.7	1.7	13.7	564.0	534	514.9	0.0	2.0
612.9	–	562.3	0.5	0.0	600.1	558	635.2	0.7	2.6
636.3	583	598.9	1.6	123.2	723.4	662	664.5	3.6	4.9
669.0	–	635.1	2.7	0.0	746.4	696	715.5	0.5	74.0
697.2	647	643.9	0.3	64.3	781.9	728	752.7	0.3	9.0
706.0	647	653.3	0.0	53.6	855.6	763	772.3	0.4	47.0
769.3	692	731.3	21.5	29.4	856.0	763	796.6	16.7	15.5
786.5	705	732.0	0.5	79.6	872.5	823	821.7	4.2	18.5
840.2	751	770.9	0.0	76.9	953.3	856	866.7	1.9	8.1
871.0	–	825.3	0.6	0.0	963.8	856	879.2	0.0	20.0
937.5	855	878.3	0.3	4.8	1094.3	–	912.4	3.6	0.6
960.8	890	883.9	1.3	4.1	1098.5	1014	982.6	0.1	0.6
1067.6	–	981.9	0.1	0.0	1140.9	1014	1000.7	54.5	0.1
1085.5	987	1014.5	34.9	9.8	1155.5	1084	1091.4	10.0	11.3
1128.4	–	1041.9	0.0	0.2	1248.8	1150	1153.3	2.3	0.1
1173.8	1082	1099.2	2.6	103.7	1282.9	1186	1174.4	0.3	13.6
1214.4	1151	1130.5	0.8	41.4	1288.2	1186	1188.2	21.2	15.1
1223.7	–	1143.4	0.3	272.8	1322.2	1200	1251.2	1.8	2.9
1235.4	1178	1176.4	5.0	0.9	1445.1	1382	1348.7	6.4	564.8
1328.6	1260	1217.8	3.0	18.8	1464.8	1382	1365.5	28.9	50.0
1338.1	1275	1231.1	50.8	166.6	1569.4	1445	1411.7	3.6	28.1
1340.0	1275	1318.6	2.0	7.3	1600.5	1466	1446.9	0.6	13.3
1529.6	1341	1379.5	4.1	64.8	1718.9	1567	1585.6	12.3	71.3
1551.1	1387	1405.7	31.5	191.1	1741.9	1598	1593.8	43.9	70.1
1582.7	1422	1455.6	1.4	14.6	1783.0	1609	1634.9	13.1	730.4
1632.0	1470	1488.0	11.9	0.1	1827.1	1623	1637.0	34.1	360.4
1722.8	1571	1614.2	43.3	1.7	3297.8	3036	3097.7	252.1	84.1
1742.2	1576	1618.8	52.4	4.7	3425.7	3110	3179.9	51.3	19.2
1892.9	1700	1779.4	8.9	531.2	3429.9	3110	3182.1	187.0	29.6
1898.6	1710	1783.8	139.6	130.9					
3391.8	3070	3191.5	89.5	4.7					
3424.2	3102	3219.2	42.9	1.3					
3428.0	3115	3221.7	158.5	0.8					
3991.4	3479	3761.3	95.1	108.9					
3991.6	3520	3761.7	185.0	92.1					

CASSCF and experimental frequencies are taken from [3] and [10], respectively.

1143 cm⁻¹, and the O–H bend mode at about 599 cm⁻¹, while the IR experiment for DPA in water [10] shows the most intense IR frequencies at 3479, 1700, 1275, 1151, and 583 cm⁻¹. The most intense calculated Raman-active frequencies for DPA correspond to the O–H stretch mode near 3761 cm⁻¹, the C–H stretch mode near 3222 cm⁻¹, and the C=O stretch mode at about 1784 cm⁻¹, while the Raman experiment for DPA in water [10] shows the most intense Raman-active frequencies at 3115 and 1710 cm⁻¹. A similar analysis can be given for DPA⁻².

This detailed comparison at first does not seem to indicate good agreement between the calculated and experimental frequencies for the O–H stretch, O–H bend, C=O stretch, C–H bend, and C–H stretch modes. Recall, however, that the theory is for molecules in the gas phase, whereas the experiments involve molecules in solution. As discussed in Section 6, the differences are caused by the interaction of the carboxyl group and H with the surrounding water molecules in the experimental systems. We will see that inclusion of solute–solvent interaction in

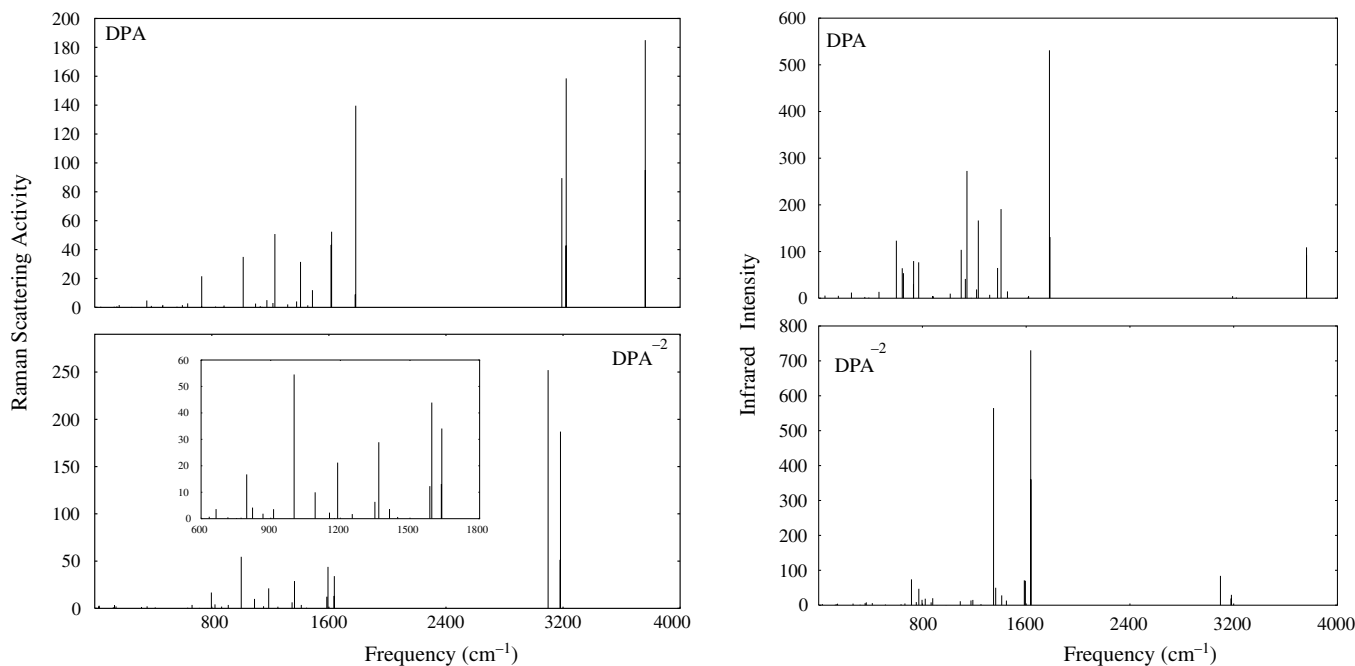


Fig. 2. B3LYP/6-311+G(2df,2pd) calculations of Raman scattering activities (I_r) and infrared intensities (I_{ir}) for DPA and DPA dianion.

the theoretical model yields theoretical frequencies which compare somewhat more favorably with experiment.

4. Nuclear magnetic shielding tensors

Nuclear magnetic resonance (NMR) provides a capability for investigating molecular mobility in structural spore compartments, non-invasively and in vivo. The ^{13}C NMR spectra have been reported for crystalline and amorphous DPA [20], but there have not yet been corresponding theoretical studies to help in interpreting the data. This provides motivation for studying the second-order magnetic response of DPA and DPA^{-2} .

There are a number of theoretical methods for calculating this second-order magnetic response in molecules. It has been shown that gauge-invariant procedures (GIPs) [15] are required to predict these properties accurately with a finite basis. In this paper, we focus on two GIPs [18] for predicting NMR shielding tensors at the DFT level of theory. They are, respectively, based on gauge-including atomic orbitals (GIAO) and a continuous set of gauge transformations (CSGT). The GIAO and CSGT procedures achieve gauge invariance in different ways. The GIAO method uses basis functions having an explicit field dependence, whereas the CSGT method is based on gauge transformations. More details for both methods can be found, for example, in the work of Cheeseman et al. [21].

The nuclear magnetic shielding isotropy σ is defined as [18]

$$\sigma = (\sigma_{xx} + \sigma_{yy} + \sigma_{zz})/3, \quad (4.1)$$

where σ_{ij} ($i, j = x, y, z$) is a component of the shielding tensor. The shielding anisotropy $\Delta\sigma$, an indication of the quality of the magnetic shielding tensor, is defined as [18]

$$\Delta\sigma = \sigma_3 - (\sigma_1 + \sigma_2)/2, \quad (4.2)$$

where $\sigma_1 < \sigma_2 < \sigma_3$ are the eigenvalues of the shielding tensor. In an experiment, the nuclear magnetic shielding difference δ , called the chemical shift, is measured in parts per million (ppm) and is given by [18]

$$\delta = (\sigma^r - \sigma^s) \times 10^6, \quad (4.3)$$

where σ^r and σ^s denote the shielding isotropies σ for the reference and sample, respectively.

Here, we perform B3LYP hybrid DFT calculations of the nuclear magnetic shielding tensor for carbon, nitrogen, oxygen, and hydrogen atoms in DPA and DPA^{-2} , by using the GIAO and CSGT methods with different bases. Each calculation is performed with a specific basis set, using the geometry optimized with the same basis. The detailed results are summarized in Table 6.

The NMR shielding tensors for both DPA and DPA^{-2} separate into 4 spectral lines for ^{13}C , 2 for ^{17}O , and 1 for ^{15}N . ^1H gives rise to 3 spectral lines in DPA, and 2 in DPA^{-2} . In the experiments [20], four ^{13}C NMR spectral lines are observed, and are generally designated α for the C3 and C4 sites, β for C5 and C6, γ for C2, and ‘‘carboxyl’’ for C9 and C10. These same four lines are seen in our calculations.

Our results also demonstrate the convergence of the GIAO and CSGT procedures with respect to the size of the basis set, when absolute shielding constants are computed using B3LYP hybrid DFT methods. The shielding constants calculated with the GIAO and CSGT methods are found to converge to almost the same values for the largest basis set 6-311+G(2df,2dp). However, it should be noted that CSGT costs far more CPU time than GIAO on the same machine. For example, in the Sun Fire Cluster

Table 6

B3LYP/6-311+G(2df,2pd) calculations of the absolute isotropy (σ , in ppm) and anisotropy ($\Delta\sigma$, in ppm) of the carbon, nitrogen, oxygen, and hydrogen shielding tensors in DPA and DPA⁻² using the GIAO and CSGT methods

NMR signal	DPA				DPA ⁻²			
	CSGT		GIAO		CSGT		GIAO	
	σ	$\Delta\sigma$	σ	$\Delta\sigma$	σ	$\Delta\sigma$	σ	$\Delta\sigma$
α : {C3,C4}	30.5 (30.8, 30.8)	151.3 (150.7, 150.6)	30.1	150.4	7.4	196.9	6.9	197.2
β : {C5,C6}	49.1 (47.2, 47.3)	199.1 (202.8, 202.5)	49.0	198.4	62.5	154.2	62.5	152.9
Carboxyl: {C9,C10}	11.8 (9.1, 9.2)	86.3 (92.3, 92.2)	11.1	86.6	3.7	94.8	3.3	93.9
γ : {C2}	42.1 (38.2, 38.4)	202.9 (212.0, 211.4)	41.6	202.5	52.0	169.9	51.6	169.3
{N1}	-101.9 (-87.8, -90.2)	580.1 (555.2, 559.6)	-102.6	580.4	-93.7	537.6	-95.8	540.3
{O11,O12}	-71.4 (-42.3, -43.3)	531.0 (500.7, 501.4)	-72.4	532.2	3.6	336.4	2.7	339.1
{O13,O14}	128.9 (130.8, 130.4)	166.4 (142.7, 143.9)	126.6	167.9	-7.3	393.7	-7.3	395.7
{H7,H8}	23.1 (22.8, 22.8)	8.2 (8.2, 8.2)	22.9	8.4	24.6	8.0	24.5	8.1
{H16,H17}	25.5 (22.7, 22.9)	10.5 (11.8, 11.7)	25.3	10.2				
{H15}	23.6 (23.0, 23.1)	6.0 (6.0, 6.0)	23.6	6.0	25.9	5.2	24.9	5.2

The values in parentheses are computed for DPA in water (first number) and in ethanol (second number), respectively.

of the High Performance Computing Virtual Laboratory (<http://www.hpcvl.org/>) located at Queen's University, CSGT/6-311+G(2df,2pd) and GIAO/6-311+G(2df,2pd) calculations using 8 processors took about 140 and 90 min, respectively. Similar results were obtained for fullerenes [18]. This suggests that GIAO may be the method of choice for molecules like those considered here.

NMR chemical shifts, as opposed to absolute shielding constants σ , are measured with high accuracy in applications of NMR spectroscopy. The calculated chemical shifts should be in better agreement with experiment, therefore, if one compares differences rather than absolute values [21]. In the experiments [20], the α , β , γ , and carboxyl NMR signals for DPA have chemical shifts of 149.8, 128.1, 138.8, and 171.0 ppm with respect to ¹³C in tetramethylsilane (TMS). Thus, relative to the carboxyl NMR signal, the α , β , and γ signals are shifted by 20, 42, 31 ppm. These values are in excellent agreement with our calculated shifts of 19, 38, 31 ppm when B3LYP/6-311+G(2df,2dp) is used, as shown in Fig. 3.

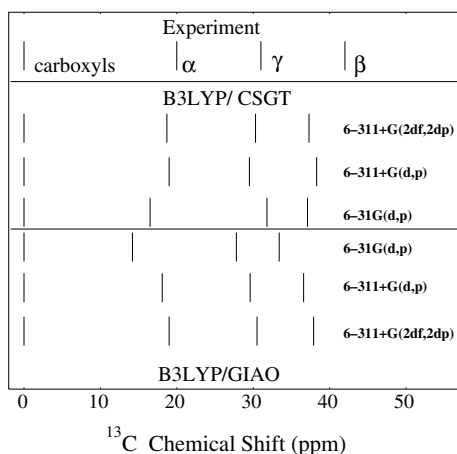


Fig. 3. Chemical shifts of α , β , and γ NMR signals with respect to the carboxyl signal in DPA, calculated using B3LYP/CSGT and B3LYP/GIAO with 6-31G, 6-31G(d,p), 6-311+G(d,p), and 6-311+G(2df,2dp) basis sets. The experimental results are taken from [20].

Nuclear magnetic shielding anisotropies $\Delta\sigma$ are also presented in Table 6. These quantities ordinarily cannot be measured in the gas phase. However, they can be determined with solid state NMR, a spectroscopic technique that can be employed for bulk materials and for surfaces and interfaces [22]. This technique is therefore appropriate for bacterial spores which contain proteins, polysaccharides, phosphorus, or solid DPA [22]. The main advantage of NMR is its selectivity, a feature that may be useful in the identification of bacterial spores.

5. Optical excitation and absorption spectra

TD-DFT is a widely used computational technique for treating electronic excitations. It incorporates screening and relevant correlation effects, and has been successfully applied to the excitation energies and photoabsorption spectra of atoms, molecules, and clusters [12,23–25]. Here, we apply TD-DFT in computing the optical excitation and absorption spectra of DPA and DPA⁻². We find that our results successfully explain the measured near ultraviolet absorption spectrum of DPA and DPA⁻².

We use the optimized ground-state structures discussed in Section 2, together with the adiabatic approximation and the static hybrid B3LYP functional. We compute the energy ${}^{(1)}E_i$ (${}^{(3)}E_i$) of the i th singlet (triplet) excited state, and the oscillator strengths f_{osc} . The optical absorption gap E_{og} , discussed below, is defined to be the excitation energy for the first dipole-allowed transition of an atom or molecule.

Since the calculated excitation energies may be useful in assisting with the development of spectroscopic techniques for identification of bacterial spores, we list in Table 7 the first 40 singlet excitation energies ${}^{(1)}E_i$ ($i = 1, \dots, 40$), and the oscillator strengths f_{osc} , for both DPA and DPA⁻². We find that the excitation energies are converged when the basis set is increased up to 6-311+G(2df,2pd). In Fig. 4, we show the near ultraviolet absorption spectra for both DPA and DPA⁻². The absorption spectra for

Table 7
Excitation energies (given by wavelengths in nm) and oscillator strengths for excitations in DPA and its dianion, calculated using TD-DFT with B3LYP functional, and 6-311+G(2df,2pd) basis set

DPA (gas)		DPA in water		DPA in ethanol		DPA dianion	
λ	f_{osc}	λ	f_{osc}	λ	f_{osc}	λ	f_{osc}
300.82	0.0000	290.79 (-10.03)	0.0017	292.11 (-8.71)	0.0017	366.80	0.0008
297.87	0.0013	288.77 (-9.10)	0.0000	290.71 (-7.16)	0.0000	348.85	0.0034
262.65	0.0001	253.61 (-9.04)	0.0002	254.20 (-8.45)	0.0001	345.52	0.0007
257.77	0.0000	251.80 (-5.97)	0.0010	252.02 (-5.75)	0.0000	336.49	0.0010
245.60	0.0723	248.75 (3.15)	0.1174	248.62 (3.02)	0.1173	326.05	0.0129
230.72	0.0919	233.51 (2.79)	0.1170	233.59 (2.87)	0.1208	314.59	0.0540
227.14	0.0000	219.62 (-7.52)	0.0000	220.18 (-6.96)	0.0000	313.47	0.0025
224.27	0.0006	219.14 (-5.13)	0.0007	219.37 (-4.90)	0.0007	308.87	0.0009
200.45	0.4960	206.00 (5.55)	0.7150	206.16 (5.71)	0.7268	303.22	0.0002
197.86	0.0324	203.00 (5.14)	0.1194	202.78 (4.92)	0.1171	302.57	0.0008
195.82	0.2290	192.72 (-3.10)	0.0424	192.98 (-2.84)	0.0489	300.74	0.0041
193.91	0.0239	191.78 (-2.13)	0.0066	191.88 (-2.03)	0.0106	295.28	0.0214
191.90	0.0002	190.63 (-1.27)	0.0415	190.69 (-1.21)	0.0347	294.86	0.0001
190.03	0.1203	189.07 (-0.96)	0.1366	189.27 (-0.76)	0.1345	294.68	0.0250
189.39	0.0002	185.20 (-4.19)	0.0004	185.95 (-3.44)	0.0004	290.28	0.0020
185.81	0.0348	181.29 (-4.52)	0.0118	182.01 (-3.80)	0.0127	282.40	0.0012
177.16	0.0002	175.09 (-2.07)	0.0000	175.16 (-2.00)	0.0000	282.02	0.0159
176.10	0.0000	171.88 (-4.22)	0.0004	172.08 (-4.02)	0.0000	276.90	0.0019
175.80	0.0000	171.15 (-4.65)	0.0086	171.66 (-4.14)	0.0056	271.62	0.0036
173.08	0.0184	171.01 (-2.07)	0.0011	170.94 (-2.14)	0.0010	271.16	0.0040
170.03	0.0016	170.22 (0.19)	0.0073	170.37 (0.34)	0.0105	262.11	0.0008
169.21	0.0113	169.26 (0.05)	0.0000	168.99 (-0.22)	0.0000	260.50	0.0007
168.94	0.0005	164.44 (-4.50)	0.0013	164.94 (-4.00)	0.0010	258.65	0.0015
166.23	0.0000	163.79 (-2.44)	0.0082	164.69 (-1.54)	0.0088	257.96	0.0091
165.04	0.0804	162.72 (-2.32)	0.0033	162.90 (-2.14)	0.0031	253.91	0.0006
165.02	0.0008	160.21 (-4.81)	0.0183	160.51 (-4.51)	0.1108	253.80	0.0193
164.01	0.0000	160.10 (-3.91)	0.1029	160.31 (-3.70)	0.0135	252.96	0.0062
162.90	0.0001	159.97 (-2.93)	0.0001	159.95 (-2.95)	0.0000	251.84	0.0002
161.44	0.0002	159.70 (-1.74)	0.0019	159.92 (-1.52)	0.0017	248.54	0.0832
160.26	0.0191	159.24 (-1.02)	0.0000	159.47 (-0.79)	0.0000	247.38	0.0017
159.95	0.0021	159.18 (-0.77)	0.0000	159.16 (-0.79)	0.0002	244.34	0.0181
158.67	0.0158	155.14 (-3.53)	0.0015	155.81 (-2.86)	0.0022	241.33	0.0238
157.65	0.0000	154.56 (-3.09)	0.0004	155.01 (-2.64)	0.0000	236.41	0.0066
156.26	0.0006	154.39 (-1.87)	0.2060	154.60 (-1.66)	0.1794	236.15	0.0027
156.13	0.0034	153.21 (-2.92)	0.0007	153.76 (-2.37)	0.0003	234.17	0.0066
155.90	0.0000	152.91 (-2.99)	0.0097	153.60 (-2.30)	0.0373	234.01	0.0058
155.04	0.0000	151.75 (-3.29)	0.0033	151.87 (-3.17)	0.0192	232.35	0.0020
153.02	0.0050	151.37 (-1.65)	0.0015	151.75 (-1.27)	0.0036	230.63	0.0107
152.98	0.0000	151.36 (-1.62)	0.0059	151.69 (-1.29)	0.0077	229.75	0.0005
152.63	0.1460	151.29 (-1.34)	0.0203	151.26 (-1.37)	0.0000	229.43	0.0060

The solvent effect is modeled by the PCM model. The values in parentheses are the shifts ($X_{\text{solvent}} - X_{\text{gas}}$) relative to the gas phase.

different bases show similar spectral features, and are converged with this largest basis set.

The first singlet excited state mainly represents excitation of a single electron from HOMO to LUMO. However, this lowest singlet state for DPA is dipole-forbidden, and the first dipole-allowed transition is to the second singlet excitation. When 6-311+G(2df,2pd) is used, the optical gap of DPA is located at 298 nm, 3 nm blue-shifted relative to the first singlet excitation. However, this first dipole-allowed absorption is still very weak ($f_{\text{osc}} = 0.0013$). This fact probably explains why no absorption above 290 nm was previously observed in experiment [26]. It was reported that DPA gives emission at 333 nm [3] for excitation at 277.8 nm. This finding is in good agreement with our calculated optical gap, if the correction caused by the Stokes

shift is included. Because of the poor solubility of DPA in water, Alimova et al. [28] have recently dissolved DPA in ethanol for absorption and fluorescence measurements. It is interesting that they observe a weak absorption band in the 330–400-nm region, with two peaks at 355 and 372 nm. Moreover, when excited in this region, they found that the DPA fluoresced in the blue with two distinct emission peaks at 408 and 430 nm [28]. Based on our theoretical results, both weak absorptions do not appear to involve singlet–singlet transitions. There are two possibilities: (1) chelates with impurity ions or (2) a direct singlet–triplet excitation process.

Here we only discuss possibility (2). It is well known that benzene has extremely weak absorption at 340 nm via a direct singlet–triplet process [29]. Motivated by this result, we

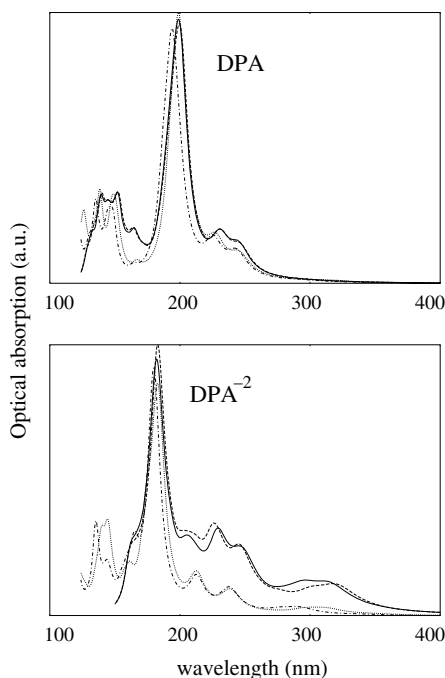


Fig. 4. Photoabsorption spectrum for both DPA and DPA^{-2} , calculated using TD-B3LYP with different basis sets: 6-31G (dotted line), 6-31G(d,p) (dot-dashed line), 6-311+G(d,p) (dashed line), and 6-311+G(2df,2pd) (solid line). All spectra were broadened to simulate finite temperature.

computed the triplet excitation energies for DPA. We find that the triplet energies below the lowest singlet energy (computed with 6-311+G(2df,2pd)) are located at 318, 352, and 355 nm. Our results then do lend support to interpretation (2) above.

In addition to the weak singlet–singlet absorption just below 300 nm for DPA, our calculated near ultraviolet absorption spectra in Fig. 4 show three major absorption bands. The first is a broad band with maxima at 245.6 and 230.7 nm. The second band is more intense and has a maximum at 200.5 nm. The third band, located at 152.6 nm, is stronger than the first band but weaker than the second. In experiment [11,26,27], as shown in Fig. 5, DPA shows a broad absorption band with maxima at 270, 273, and 279 nm, and a intense absorption peak at 215 nm. These features appear to be in reasonable agreement with our calculations, when one recognizes that DFT does not give quantitative values for excitation energies.

For DPA^{-2} , the lowest singlet state is dipole-allowed. The optical gap of DPA^{-2} predicted with 6-311+G(2df,2pd) is thus 366.8 nm, with oscillator strength $f_{\text{osc}} = 0.0008$. The second singlet state is also dipole-allowed, with a wavelength of 348.9 nm, and its oscillator strength is 4 times larger than that of the lowest singlet state. A recent fluorescence experiment [27] reported that DPA^{-2} has a very low fluorescence emission, with a maximum at 400 nm when excited at the wavelength of 300 nm. This agrees with our calculation when the Stokes shift correction is included.

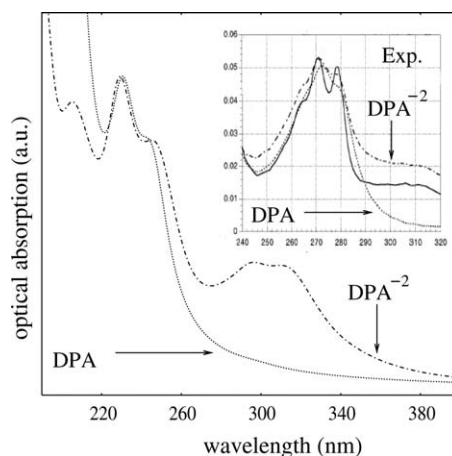


Fig. 5. Photoabsorption spectrum for both DPA and DPA^{-2} calculated by TD-B3LYP/6-311+G(2df,2pd). All spectra were broadened to simulate finite temperature. The inset shows the experimental spectra, adapted from [27].

The near ultraviolet spectrum for DPA^{-2} , shown in Fig. 4, has four absorption bands. The first is a broad band, with maxima at 326.1, 314.6, 295.2, 294.7, and 282.0 nm. The second is also a broad band, with maxima at 253.8, 248.5, and 241.3 nm. The third band is the strongest and has a maximum at 181.6 nm. The fourth is also strong, with a maximum at 130 nm. In a recent experiment for DPA^{-2} [27], as shown in Fig. 5, the spectrum contains a broad absorption band in the 300–320-nm region, and two distinct absorption peaks at 278 and 271 nm, with a shoulder at 263 nm. These features appear to agree quite well with our calculations.

6. Solvent effects on the spectral properties of DPA

In the above sections, we have shown that DFT provides reliable results for the isolated DPA molecule in the gas phase. However, since IR, Raman, near ultraviolet, and NMR spectra are often measured in condensed phases, environmental factors may affect the spectral properties. For example, some of the IR and Raman experiments on DPA are performed in water solutions [10] and in thin films [5]. Thus, to elucidate the measured spectra, theoretical methodologies need to take account of environmental factors. In this section, we discuss solvent effects.

Various theoretical approaches have been proposed for the treatment of solvent effects on spectral properties of molecules. A microscopic point of view suggests a supermolecule description [30] or the use of statistical mechanical simulation techniques in conjunction with quantum chemistry methods [31]. Both of these approaches have disadvantages, however: The supermolecule description does not include bulk solvent effects, and the statistical procedure is prohibitively expensive. However, the polarizable continuum solvent model (PCM) [32] has been shown to be reliable and very effective in the description of solvent effects. In the PCM, the solvent is simulated as a continuous,

infinite, homogeneous, and generally isotropic dielectric medium, characterized by a dielectric constant ϵ . The advantage of the PCM technique is that we can treat a limited number of solvent molecules quantum mechanically, while the bulk of the solvent is represented by a continuum model [33]. On the other hand, there is a solvent relaxation delay following a sudden change of solute electronic density. Thus non-equilibrium effects need to be included, to describe the solvent–solute interaction, and this can be

accomplished by using the optical dielectric constant [34]. In polar environments, the non-equilibrium effect is quite important if one is to quantitatively reproduce the observed spectra. Here, we use the non-equilibrium PCM to calculate solvent effects on the spectra of DPA. The computations were performed using the Gaussian03 package, including the PCM implementation, and the ground-state molecular structures were optimized with 6-311+G(2df,2pd).

Table 8

Quantities calculated for DPA in water and ethanol, using B3LYP/PCM/6-311+G(2df,2pd): Raman scattering activities (I_r , in 10^{-14} m⁴/kg); infrared intensities (I_{ir} , in km/mol); and vibrational frequencies (ν , in cm⁻¹)

Experimental	DPA in water			DPA in ethanol		
	ν	I_r	I_{ir}	ν	I_r	I_{ir}
79	42.0 (0.8)	2.7 (2.2)	0.0 (0.0)	45.3 (4.1)	2.5 (2.0)	0.0 (0.0)
79	57.0 (8.1)	0.0 (0.0)	17.1 (11.6)	61.4 (12.5)	0.0 (0.0)	15.6 (10.1)
107	122.6 (−10.3)	0.1 (−0.3)	6.6 (6.4)	119.9 (−13.0)	0.1 (−0.4)	6.1 (5.9)
218	150.0 (−1.4)	6.2 (5.6)	12.0 (6.9)	150.6 (−0.8)	5.5 (4.8)	11.9 (6.7)
–	159.9 (−7.4)	7.9 (6.3)	0.0 (0.0)	160.9 (−6.4)	7.3 (5.8)	0.0 (0.0)
252	250.5 (−1.7)	0.4 (0.1)	45.8 (33.7)	249.4 (−2.8)	0.5 (0.1)	43.2 (31.0)
330	353.6 (−2.4)	15.6 (10.8)	3.0 (0.4)	353.9 (−2.1)	15.0 (10.3)	3.1 (0.4)
365	380.5 (−6.5)	0.7 (−0.4)	0.8 (−0.6)	380.8 (−6.2)	0.6 (−0.4)	0.7 (−0.6)
421	429.6 (−5.4)	0.0 (0.0)	0.6 (0.4)	430.7 (−4.4)	0.0 (0.0)	0.6 (0.4)
–	459.9 (−4.3)	1.8 (1.3)	3.3 (3.3)	461.2 (−3.0)	0.7 (0.2)	0.4 (0.4)
–	463.8 (−0.8)	4.7 (3.0)	11.5 (−2.1)	462.6 (−2.1)	5.6 (3.9)	14.6 (1.0)
–	562.5 (0.2)	2.2 (1.8)	107.3 (107.3)	562.8 (0.5)	2.1 (1.6)	6.5 (6.5)
583	563.1 (−35.8)	2.4 (0.8)	188.4 (65.2)	566.8 (−32.1)	2.3 (0.7)	273.2 (150.0)
–	596.3 (−38.8)	5.0 (2.3)	0.0 (0.0)	600.1 (−35.0)	4.7 (2.0)	0.0 (0.0)
647	639.9 (−3.9)	1.5 (1.2)	113.3 (49.0)	639.5 (−4.4)	1.3 (1.0)	111.2 (47.0)
647	655.1 (1.8)	0.0 (0.0)	67.0 (13.4)	654.8 (1.5)	0.0 (0.0)	66.9 (13.3)
692	724.5 (−6.8)	0.6 (−20.9)	125.2 (95.8)	725.9 (−5.4)	0.5 (−21.0)	119.3 (89.9)
705	732.1 (0.1)	59.8 (59.3)	64.2 (−15.4)	732.0 (0.0)	56.5 (56.0)	62.9 (−16.7)
751	763.3 (−7.6)	0.3 (0.2)	116.9 (40.0)	764.4 (−6.6)	0.2 (0.2)	115.2 (38.3)
–	825.9 (0.6)	4.2 (3.6)	0.0 (0.0)	826.4 (1.1)	3.6 (3.0)	0.0 (0.0)
855	878.9 (0.7)	2.8 (2.4)	7.3 (2.5)	878.7 (0.4)	2.4 (2.0)	7.0 (2.2)
890	882.9 (−1.1)	6.9 (5.6)	10.2 (6.1)	883.3 (−0.7)	6.6 (5.3)	9.7 (5.6)
–	976.0 (−5.9)	1.3 (1.1)	0.0 (0.0)	977.2 (−4.7)	1.3 (1.1)	0.0 (0.0)
987	1007.6 (−6.9)	131.9 (97.0)	40.6 (30.8)	1007.5 (−7.0)	122.7 (87.8)	38.6 (28.9)
–	1043.9 (2.1)	0.1 (0.0)	0.1 (−0.1)	1044.0 (2.2)	0.1 (0.0)	0.1 (−0.1)
1082	1099.9 (0.8)	5.5 (2.9)	168.0 (64.3)	1100.4 (1.2)	5.3 (2.7)	167.0 (63.3)
1151	1130.0 (−0.5)	9.6 (8.8)	25.2 (−16.2)	1130.6 (0.0)	9.0 (8.2)	27.8 (−13.6)
–	1142.5 (−0.9)	3.3 (2.9)	568.1 (295.4)	1143.7 (0.3)	2.4 (2.1)	538.6 (265.9)
1178	1169.9 (−6.5)	15.1 (10.1)	2.6 (1.7)	1170.9 (−5.5)	14.5 (9.5)	3.0 (2.2)
1260	1206.1 (−11.7)	13.4 (10.3)	6.4 (−12.3)	1207.6 (−10.2)	13.0 (10.0)	7.5 (−11.3)
1275	1213.7 (−17.4)	187.7 (137.0)	203.6 (37.0)	1215.8 (−15.2)	178.5 (127.7)	217.3 (50.7)
1275	1310.6 (−8.0)	17.4 (15.4)	45.6 (38.3)	1311.9 (−6.7)	14.3 (12.2)	37.6 (30.3)
1341	1374.3 (−5.2)	18.5 (14.4)	141.8 (77.0)	1376.2 (−3.3)	17.5 (13.4)	135.8 (71.0)
1387	1398.8 (−6.9)	151.5 (120.1)	442.1 (251.0)	1400.6 (−5.0)	139.0 (107.5)	415.0 (224.0)
1422	1447.1 (−8.5)	2.6 (1.1)	35.5 (20.9)	1447.7 (−7.9)	2.6 (1.2)	33.4 (18.8)
1470	1485.3 (−2.7)	41.1 (29.2)	0.3 (0.3)	1485.9 (−2.1)	39.3 (27.4)	0.2 (0.1)
1571	1608.6 (−5.6)	167.8 (124.5)	0.8 (−0.9)	1608.9 (−5.3)	157.5 (114.2)	0.8 (−0.9)
1576	1615.4 (−3.5)	245.5 (193.1)	18.3 (13.6)	1615.5 (−3.4)	225.9 (173.5)	16.6 (11.9)
1700	1714.4 (−65.0)	39.4 (30.5)	1253.8 (722.6)	1717.2 (−62.2)	37.4 (28.4)	1212.3 (681.1)
1710	1722.2 (−61.7)	447.1 (307.5)	262.4 (131.5)	1724.9 (−58.9)	423.8 (284.2)	250.2 (119.3)
3070	3126.8 (−64.7)	272.0 (182.5)	0.6 (−4.1)	3131.2 (−60.3)	258.6 (169.1)	0.4 (−4.3)
3102	3157.1 (−62.1)	171.6 (128.8)	18.9 (17.6)	3161.9 (−57.3)	151.4 (108.6)	16.3 (15.0)
3115	3158.2 (−63.5)	558.7 (400.2)	6.8 (6.0)	3163.0 (−58.6)	526.4 (367.9)	5.1 (4.2)
3479	3244.0 (−517.3)	119.5 (24.5)	574.0 (465.0)	3283.4 (−478.0)	123.5 (28.4)	530.3 (421.3)
3520	3245.0 (−516.7)	380.8 (195.8)	507.3 (415.2)	3284.4 (−477.3)	372.0 (187.0)	477.1 (385.0)

The values in parentheses are the shifts ($X_{\text{solvent}} - X_{\text{gas}}$) relative to the gas phase. Experimental frequencies are taken from [10].

Note: No attempt has been made to determine the correspondence between experimental and theoretical vibrational frequencies. Instead, the theoretical frequencies simply follow the order of Table 5, so that one can observe the effect of the solvent.

The solvents we consider are water and ethanol, with static dielectric constants $\epsilon = 78.4$ and 24.6 , respectively. The computed total energies for DPA in water and ethanol are -625.689 and -625.687 hartree, which are about 0.944 and 0.879 eV lower than the values predicted in the gas phase. The isotropic static polarizabilities for DPA in water and ethanol are 143 and 141 \AA^3 , enhanced by 47% in comparison with the polarizability computed in the gas phase.

As shown in Table 2, the solvent–solute interactions (for example, hydrogen bonding) enhance the propensity for gaining (losing) electrons in the acceptor (donor) sites. Table 3 shows that the change of bond lengths (as compared with DPA in the gas phase) mainly occurs in the O–H, C=O, C–H, and C–O bonds: The O–H, double C=O, and C–H bond lengths increase by about 2.4% , 0.5% , and 0.3% , respectively, while the single C–O bond length decreases by 0.8% . Correspondingly, although it is not shown here, we observe a significant change of bond angles C–O–H (increasing by 1.6%), C2–C5–H7 and C2–C6–H8 (decreasing by 0.7%), and O=C–C (increasing by 0.3%). Thus, the solvent has a strong effect on the COOH functional group, and little effect on the ring and on the H at site 15. This is demonstrated by the computed isotropy and anisotropy of the C, H, N, and O shielding tensors

for DPA in water or ethanol, which are given in Table 6. For example, the solvent effect shifts the absolute isotropy of O at the sites 11 and 12 by about 41% , but produces little change in the shielding tensor of H at the site 15.

In Table 8, we present the vibrational frequencies, IR intensities, and Raman scattering activities of DPA in water and ethanol. We find that the solvent–solute interaction mainly results in a redshift of vibrational frequencies, compared to those predicted for the gas phase. In particular, there are significant redshifts observed in the following vibrational modes: 14% in the O–H stretch mode, 6% in the O–H bend mode, 4% in the C=O stretch mode, and 1.4% in the C–H bend mode. Inclusion of solvent effects provides for more meaningful comparison with experiment, and the values of the vibrational frequencies show somewhat better agreement. For example, the relative error between theory and experiment is reduced to 0.8% for the C=O stretch mode (compared to 4% for the gas phase prediction), 1.5% for the C–H stretch mode (compared to 4% when the gas phase prediction is used), and 6% for O–H stretch mode (compared to 8% for the gas phase prediction). As listed in Table 8, and shown in Figs. 6 and 7, the infrared intensities are enhanced greatly in the O–H stretch, C=O stretch, C–C ring stretch, and C–COOH bend modes, while

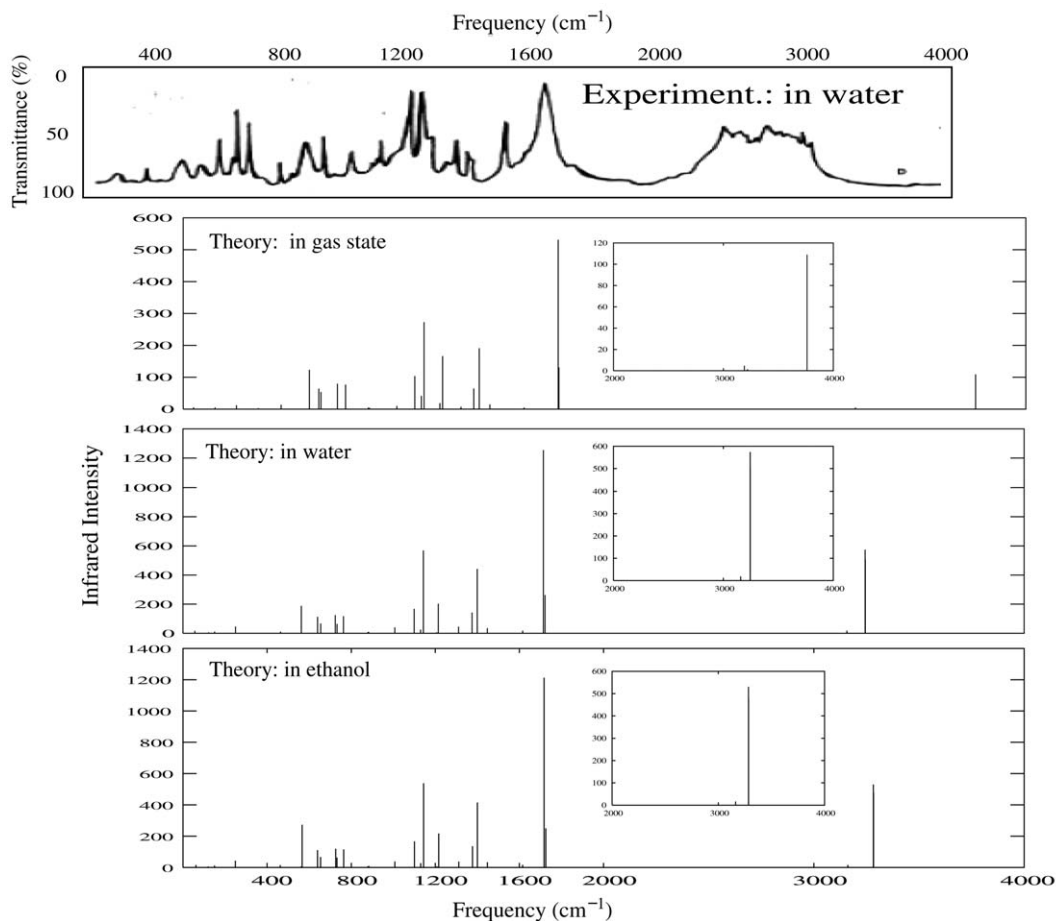


Fig. 6. B3LYP/6-311+G(2df,2pd) calculations of infrared intensity (I_{ir}) for DPA in water and ethanol, respectively. The experimental IR spectrum of DPA in water is adapted from [10].

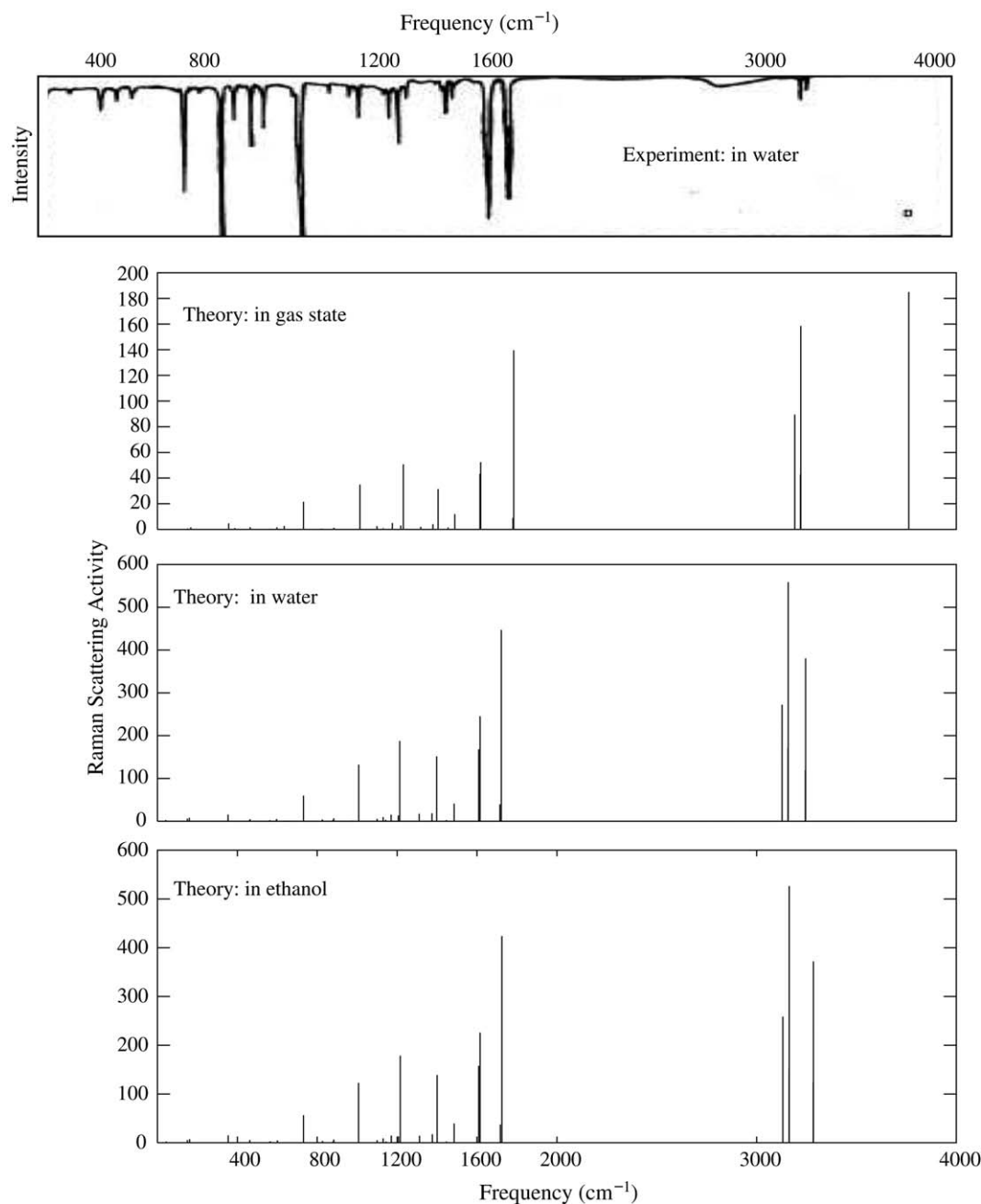


Fig. 7. B3LYP/6-311+G(2df,2pd) calculations of Raman scattering activities (I_r) for DPA in water and ethanol, respectively. The experimental Raman spectrum of DPA in water is adapted from [10].

the Raman scattering activities are enhanced greatly in the O–H, C–H, and C=O stretch modes and the C–C ring stretch and C–C-ring bend modes. The corrected IR and Raman spectra, with solvent effects included, are in reasonably good agreement with experiment [10].

Recently, Cossi and Barone [34] have applied the PCM with TD-DFT to examine solvent effects on electronic spectra, and the computed transition energies are in fairly good agreement with experimental values. Using their approach, we have computed the excitation energies of DPA in solution. Table 7 displays the first 40 vertical excitation energies for DPA in water and ethanol, respectively. Fig. 8 com-

pares the computed near ultraviolet spectra for DPA in water, in ethanol, and in the gas phase. As discussed above, a change of symmetry in the DPA is expected when the solvent–solute interaction is taken into account.

As shown in Table 7, the lowest singlet excitation for DPA in water or ethanol is optically active, with oscillator strength $f_{osc} = 0.0017$, while the lowest singlet excitation for DPA in the gas phase is dipole-forbidden. Thus, the optical gap of DPA in the gas phase (298 nm) is blueshifted by 5–7 nm due to the solute–solvent interaction. Another significant observation is found from the computed results. The solvent–solute interaction leads to a 6 nm redshift of

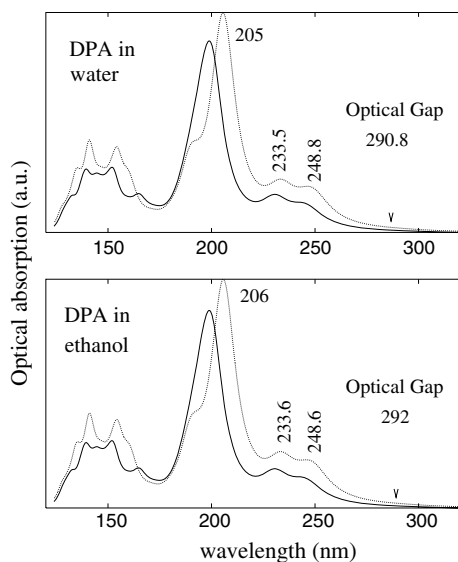


Fig. 8. Photoabsorption spectrum for DPA in water and ethanol (dotted line) calculated using TD-B3LYP/6-311+G(2df,2pd), compared with the spectrum in the gas state (solid line). All spectra were broadened to simulate finite temperature.

the strongest absorption, a 3 nm redshift of the 230–245 nm absorption band, and 1–10 nm blueshifts for other excitation energies computed in the gas phase.

7. Summary

In summary, we have performed DFT calculations of the structure, electronic properties, vibrational frequencies, IR intensities, Raman scattering activities, NMR shielding tensors, and optical excitations for both DPA and DPA⁻². Also, we included solvent effects on the spectral properties of DPA, by combining the polarizable continuum model with DFT. In each case, our calculated results are in reasonably good agreement with experiment.

Acknowledgments

This work was supported by the Robert A. Welch Foundation (Grant A-0929), and by DARPA (HR0011-04-1-0026), ONR (N00014-04-1-0336), and AFOSR (F49620-01-1-0566). V.H.S. and J.R.H.X. thank the HPCVL (High Performance Computing Virtual Laboratory) at Queen's University for the use of its parallel supercomputing facilities. V.H.S. acknowledges support from the Natural Science and Engineering Research Council of Canada (NSERC). Finally, we thank M.O. Scully for many helpful discussions.

References

[1] S. Udo, *J. Agr. Chem. Soc. Jpn.* 12 (1936) 386.
 [2] K.E. Edgecombe, D.F. Weaver, V.H. Smith Jr., *Can. J. Chem.* 72 (1994) 1388.

[3] H.F. Hameka, J.O. Jensen, J.L. Jensen, C.N. Merrow, C.P. Vlahacos, *J. Mol. Struct. (Theochem)* 365 (1996) 131.
 [4] R.P. Singh, *Curr. Sci.* 56 (1987) 1232.
 [5] A.A. Kolomenskii, S.N. Jerebtsov, T. Opatrny, H.A. Schuessler, M.O. Scully, *J. Mod. Opt.* 50 (2003) 2369.
 [6] M.O. Scully, G.W. Kattawar, R.P. Lucht, T. Opatrny, H. Pilloff, A. Rebane, A.V. Sokolov, M.S. Zubairy, *Proc. Natl. Acad. Sci. USA* 99 (2002) 10994.
 [7] (a) J.C. Lewis, *Anal. Biochem.* 19 (1967) 327;
 (b) R.R.M. Patterson, C. Kemmelmeier, *J. Chromatogr.* 511 (1990) 195.
 [8] H. Shibata, S. Yamashita, M. Ohe, I. Tani, *Microbiol. Immunol.* 30 (1986) 307.
 [9] R. Manoharan, E. Ghiamati, R.A. Dalterio, K.A. Britton, W.H. Nelson, J.F. Sperry, *J. Microbiol. Meth.* 11 (1990) 1.
 [10] P. Carmona, *Spectrochim. Acta* 36 (1979) 705.
 [11] E. Ghiamati, R. Manoharan, W.H. Nelson, J.F. Sperry, *Appl. Spectrosc.* 46 (1992) 357.
 [12] (a) E. Runge, E.K.U. Gross, *Phys. Rev. Lett.* 52 (1984) 997;
 (b) M.E. Casida, C. Jamorski, K.C. Casida, D.R. Salahub, *J. Chem. Phys.* 108 (1998) 4439;
 (c) R.E. Stratmann, G.E. Scuseria, M.J. Frisch, *J. Chem. Phys.* 109 (1998) 8218.
 [13] A.D. Becke, *J. Chem. Phys.* 98 (1993) 5648.
 [14] W. Kolos, C.C.J. Roothaan, *Rev. Mod. Phys.* 32 (1960) 219.
 [15] M.J. Frisch, G.W. Trucks, H.B. Schlegel, G.E. Scuseria, M.A. Robb, J.R. Cheeseman, J.A. Montgomery Jr., T. Vreven, K.N. Kudin, J.C. Burant, J.M. Millam, S.S. Iyengar, J. Tomasi, V. Barone, B. Mennucci, M. Cossi, G. Scalmani, N. Rega, G.A. Petersson, H. Nakatsuji, M. Hada, M. Ehara, K. Toyota, R. Fukuda, J. Hasegawa, M. Ishida, T. Nakajima, Y. Honda, O. Kitao, H. Nakai, M. Klene, X. Li, J.E. Knox, H.P. Hratchian, J.B. Cross, C. Adamo, J. Jaramillo, R. Gomperts, R.E. Stratmann, O. Yazyev, A.J. Austin, R. Cammi, C. Pomelli, J.W. Ochterski, P.Y. Ayala, K. Morokuma, G.A. Voth, P. Salvador, J.J. Dannenberg, V.G. Zakrzewski, S. Dapprich, A.D. Daniels, M.C. Strain, O. Farkas, D.K. Malick, A.D. Rabuck, K. Raghavachari, J.B. Foresman, J.V. Ortiz, Q. Cui, A.G. Baboul, S. Clifford, J. Cioslowski, B.B. Stefanov, G. Liu, A. Liashenko, P. Piskorz, I. Komaromi, R.L. Martin, D.J. Fox, T. Keith, M.A. Al-Laham, C.Y. Peng, A. Nanayakkara, M. Challacombe, P.M.W. Gill, B. Johnson, W. Chen, M.W. Wong, C. Gonzalez, J.A. Pople, *Gaussian 03, Revision C.02*, Gaussian, Inc, Wallingford, CT, 2004.
 [16] G. Strahs, R.E. Dickerson, *Acta Crystallogr. B* 24 (1968) 571.
 [17] E.B. Wilson, J.C. Decius, P.C. Cross, *Molecular Vibrations*, McGraw-Hill, New York, 1955.
 [18] R.H. Xie, G.W. Bryant, L. Jensen, J. Zhao, V.H. Smith Jr., *J. Chem. Phys.* 118 (2003) 8621.
 [19] R.H. Xie, G.W. Bryant, V.H. Smith Jr., *Phys. Rev. B* 67 (2003) 155404.
 [20] (a) R.E. Lundin, L.E. Sacks, *Appl. Environ. Microbiol.* 54 (1988) 923;
 (b) S. Ablett, A.H. Darke, P.J. Lillford, D.R. Martin, *Int. J. Food Sci. Technol.* 34 (1999) 59.
 [21] J.R. Cheeseman, M.J. Frisch, G.W. Trucks, T.A. Keith, *J. Chem. Phys.* 104 (1996) 5497.
 [22] R.G.K. Leuschner, P.J. Lillford, *Int. J. Food Microbiol.* 63 (2001) 35.
 [23] R.H. Xie, G.W. Bryant, G. Sun, M.C. Nicklaus, D. Heriger, T. Frauenheim, M.R. Manaa, V.H. Smith Jr., Y. Araki, O. Ito, *J. Chem. Phys.* 120 (2004) 5133.
 [24] R.H. Xie, G.W. Bryant, G. Sun, T. Kar, Z. Chen, V.H. Smith Jr., Y. Araki, N. Tagmatarchis, H. Shinohara, O. Ito, *Phys. Rev. B* 69 (2004) 201403(R).
 [25] R.H. Xie, G.W. Bryant, C.F. Cheung, V.H. Smith Jr., J. Zhao, *J. Chem. Phys.* 121 (2004) 2849.
 [26] R.J. Moser, E.V. Brown, *Trans. KY Acad. Sci.* 33 (1972) 65.
 [27] R. Nudelman, B.V. Bronk, S. Efrima, *Appl. Spectrosc.* 54 (2000) 445.
 [28] A. Alimova, A. Katz, H.E. Savage, M. Shah, G. Minko, D.V. Will, R.B. Rosen, S.A. McCormick, R.R. Alfano, *Appl. Opt.* 42 (2003) 4080.

- [29] I. Weinryb, R.F. Steiner, in: I. Weinryb, R.F. Steiner (Eds.), *Excited States of Proteins and Nucleic Acids*, Plenum, New York, 1971, p. 277.
- [30] M. Kraus, S.P. Webb, *J. Chem. Phys.* 107 (1997) 5771.
- [31] S.E. de Bolt, P.A. Kollman, *J. Am. Chem. Soc.* 112 (1990) 7515.
- [32] S. Miertus, E. Scrocco, J. Tomasi, *Chem. Phys.* 55 (1981) 117.
- [33] N. Rega, M. Cossi, V. Barone, *J. Am. Chem. Soc.* 119 (1997) 12692.
- [34] M. Cossi, V. Barone, *J. Chem. Phys.* 115 (2001) 4708.